forests

Article

Mapping Tree Mortality Caused by Siberian Silkmoth Outbreak Using Sentinel-2 Remote Sensing Data

Olga A. Slinkina *, Pavel V. Mikhaylov, Svetlana M. Sultson, Denis A. Demidko *, Natalia P. Khizhniak and Andrey I. Tatarintsev

Scientific Laboratory of Forest Health, Reshetnev Siberian State University of Science and Technology, Krasnoyarsk 660037, Russia; mihaylov.p.v@mail.ru (P.V.M.); sultson2011@yandex.ru (S.M.S.); natalia.melnichenko@mail.ru (N.P.K.); tatarintsevai@sibsau.ru (A.I.T.)

* Correspondence: sloa@mail.ru (O.A.S.); sawer_beetle@mail.ru (D.A.D.); Tel.: +7-913-534-40-90 (O.A.S.); +7-923-317-18-98 (D.A.D.)

Abstract: The Siberian silkmoth is one of the most dangerous coniferous forests pests. Siberian silkmoth outbreaks cause massive defoliation and subsequent forest fires over vast areas. Remote forest disturbance assessments performed after an outbreak make it possible to assess carbon emissions and the potential for natural regeneration, estimate forest fire danger, and reveal the need to implement forest management practices. The goal of the present research was to investigate the use of modern satellite imagery of medium spatial resolution to estimate the percentage of dead trees in a given area. The subject of this study is the Siberian silkmoth outbreak that occurred in 2018–2020 and covered 42 thousand ha in the Irbey region of the Krasnoyarsk Krai. Imagery from the Sentinel-2/MSI sensor was used to calculate a number of spectral indices for images received before and after the outbreak. Field study data were used to create regression models relating the index values to the percentage of dead trees. A number of spectral indices, such as NDVI, dNDVI, NBR, dNBR, NDMI, EVI, and TCG, were used. As a result, spectral indices based on the data from NIR/SWIR bands (NBR, NDMI, dNBR) demonstrated the best correlations with field-measured tree mortality. Therefore, these indices may be used to accurately estimate the percentage of dead trees by remote sensing data. The best was the NBR index with an R^2 equal to 0.87, and the lowest RMSE and MAE errors. Consequently, Sentinel-2 imagery can be successfully used for tree mortality assessment over large inaccessible areas disturbed by Siberian silkmoth outbreaks at a relatively low cost.

Keywords: Siberian silkmoth; damaged stands; remote sensing; spectral indices

Citation: Slinkina, O.A.; Mikhaylov, P.V.; Sultson, S.M.; Demidko, D.A.; Khizhniak, N.P.; Tatarintsev, A.I. Mapping Tree Mortality Caused by Siberian Silkmoth Outbreak Using Sentinel-2 Remote Sensing Data. *Forests* **2023**, *14*, 2436. https://doi.org/10.3390/f14122436

Academic Editors: Vladimir V. Shishov and Alberto Arzac

Received: 25 October 2023
Revised: 26 November 2023
Accepted: 4 December 2023
Published: 13 December 2023

1. Introduction

Boreal forests are one of the largest biomes in the world. They are dominated by coniferous stands and cover 12 million square kilometers, or about 1/3 of the planet's forests. Boreal forest zones stretch over the northern hemisphere, between 50° and 70° northern latitudes [1]. In Russia, boreal forests occupy 8.1 million square kilometers, which constitute about 2/3 of the world's boreal forests. Boreal forests play an important role in the global carbon balance by storing half of the terrestrial biosphere's carbon [2]. However, due to droughts, forest fires, pests, and other disturbances, these forests are at risk of experiencing a decline in productivity, which can cause a significant release of carbon emissions into the atmosphere.

Different climate change scenarios predict an increase in average global surface temperatures by 1.0 to 5.7 °C by the end of this century. The most dramatic changes are expected in the boreal zone, where the temperature could rise by 7 °C [3]. Large carbon pools in boreal forests are vulnerable to climate change, which calls into question the status of these forests as a carbon sink in the near future [1,4–6].

Fires and insect outbreaks are major natural disturbances of boreal forests, and they are closely interrelated. The probability of insect outbreak occurrence is significantly higher near areas where forests have been destroyed by wildfires. [7,8]. Conversely, in areas damaged by pests, the frequency of forest fires can increase up to four times compared to intact stands [9].

Forest insects can cause severe environmental changes. These include the displacement of native tree species, widespread defoliation, and mortality [10,11]. This reduces the ability of forests to capture and store carbon dioxide, and causes carbon emission release due to wood and canopy decomposition in dead stands [12]. Global warming may promote insect population growth, increase outbreak frequencies, and encourage the geographic expansion of some insect species [13–15], violating the global carbon balance.

During the last decade, about 1.5 million hectares of boreal forests have been disturbed by insect outbreaks in Siberia, primarily in Krasnoyarsk Krai (~1 million hectares). Most of these territories (~90%) were damaged by the Siberian silkmoth (*Dendrolimus sibiricus* Tschetv.) [14,16,17]. Among all the insect pests feeding on Siberian boreal forests, the Siberian silkmoth is one of the most dangerous. The Siberian silkmoth's preferred host trees are fir, Siberian pine and larch, and, to a lesser extent, spruce and Scots pine [18–21]. Outbreaks of the Siberian silkmoth cause forest dieback across vast areas. Moreover, forests disturbed by the Siberian silkmoth are at the highest risk of fire danger. Therefore, wildfires in such forests may be huge and destroy surrounding undisturbed forests in large areas [9,20,22]. Climatic changes observed in recent decades have been creating weather conditions that contribute to increases in both the area and the frequency of Siberian silkmoth outbreaks [23–26].

One of the main parameters that determines insect–pest-induced changes in forest ecosystems is the proportion of dead trees in a forest stand. Tree mortality affects forest regeneration dynamics, species composition, and the structures of both forest stands and field layers [18,20,27]. By assessing tree mortality rate, one can estimate forest fuels, and thereby predict forest fires in areas disturbed by insect pests [9,28]. What is more, assessing tree mortality rate is crucial in decision-making for sanitation cutting [29,30]. Information on tree mortality together with pre-outbreak growing stock data may be used to estimate post-outbreak carbon emissions caused by wood and canopy decomposition. Thus, quantitative assessments of the state of disturbed forest stands are important both from the environmental and economic points of view, and are one of the factors determining decision-making in forest management.

Traditional methods for estimating tree mortality involve conducting field studies. These methods have a number of disadvantages: they are time- and labor-consuming, high-cost, and usually only cover a small area. The use of satellite imagery is a resource-saving alternative that allows the coverage of vast areas that are often inaccessible for field research.

In recent years, research has been actively conducted, focused on remote forest health assessment in stands disturbed by insect pests. The potential of satellite imagery for assessing the state of plants is due to their reflectivity (albedo), which varies depending on the wavelength and the state of vegetation. In the visible part of the spectrum, the spectral properties of vegetation are mainly controlled by chlorophyll. Chlorophyll absorbs light in the blue (450–480 nm) and red (660–690 nm) regions of the spectrum. That is why green vegetation reflectance in the blue and red parts of the spectrum is low. Under stress conditions, the plant chlorophyll content decreases rapidly, leading to a decrease in absorption (and an increase in reflection) in the corresponding spectral ranges. In the near-infrared (NIR) spectrum, the reflectance of healthy vegetation is much greater than in any portion of the visible spectrum. Water has strong absorption in certain parts of the short-wave infrared (SWIR) region (1400, 1900, 2500 nm). Therefore, needle/leaf water content has a significant effect on the reflectance characteristics of vegetation in these ranges [31–34]. The reflection of radiation from vegetation in various parts of the electromagnetic spectrum are recorded by multispectral scanners on board remote sensing satellites. Albedo values determined for different spectral bands are used to calculate indices (vegetation, humidity, etc.) that indicate the state of plants' health.

A significant number of studies have shown the effectiveness of using remote sensing in assessing forest condition after various disturbances; in particular, to assess tree mortality caused by insect outbreaks. Different types of imaging sensors and various methodological approaches have been used to assess the state of damaged forest stands. According to a systematic review [34], the number of such studies has increased sharply since 2005, and most of them (about 60%) used medium resolution satellite images (mainly, Landsat imagery). Research [35–40] shows the applicability of Landsat data for characterizing forest state and assessing tree mortality caused by various types of insect pests. Low-resolution (AVHRR, MODIS) [41,42] and high- resolution satellite data are also used for such studies (HyMap, QuickBird, RadpidEye, WorldView-2) [43–45].

Sentinel-2/MSI data are relatively new to the satellite data services (the mission was launched in 2015 by European Space Agency), and are currently the best spatial and temporal resolution data available for free access. Therefore, the aim of the present study was to explore the potential of using this satellite imagery for quantitative assessments of the state of forests disturbed by Siberian silkmoth outbreaks. To achieve this goal, we plan to compare spectral indices based on the albedo of forest vegetation received from Sentinel-2 imagery with field measurements of tree mortality. Finally, we are going to identify the most suitable remote sensing index to map the state of disturbed forests.

2. Materials and Methods

2.1. Study Area

The study was carried out in Krasnoyarsk Krai, Russia. Krasnoyarsk Krai has the largest forest-growing stock in Russia, estimated at 11.7 million cubic meters. The forested area covers 1.6 million square kilometers, or ~13% of the world's boreal forests. The research was focused on studying the Siberian silkmoth outbreak that occurred in 2018–2020 and covered 42,000 ha in Irbeysky District of Krasnoyarsk Krai (Figure 1). The outbreak followed a classic evolution: it lasted three years, the first disturbances occurred in August 2018, maximum damage was observed during the summer of 2019, and the outbreak ended in June 2020.

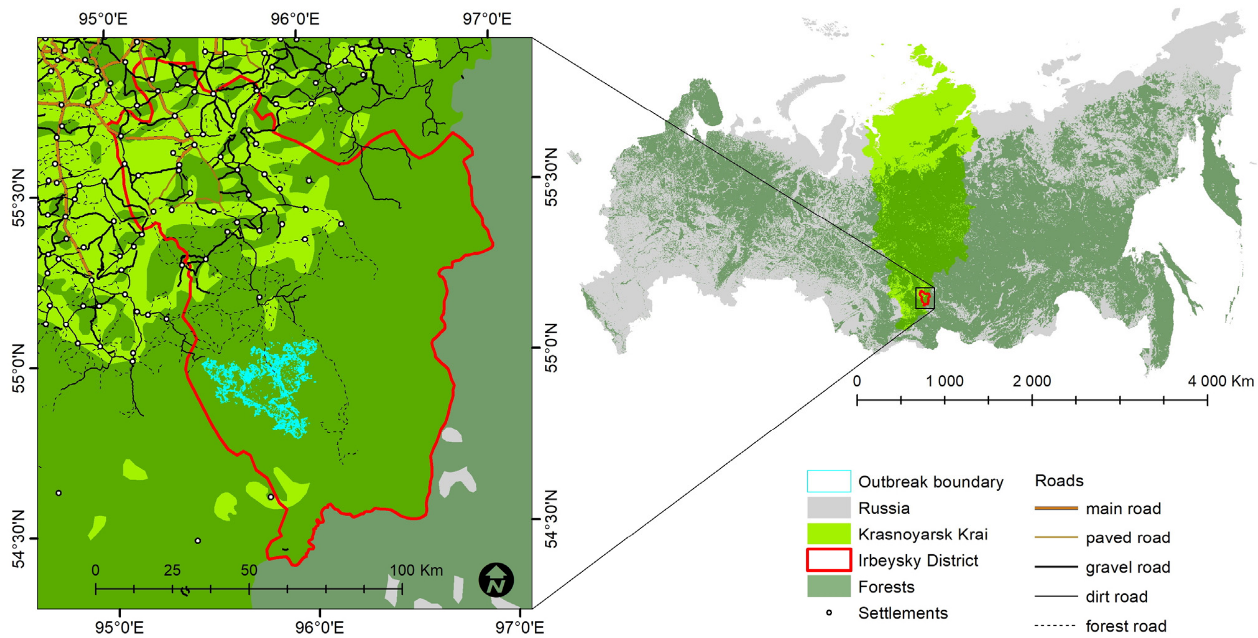

Figure 1. Study locations.

The disturbed stands are located between the Kan and Agul rivers, in a remote area with no settlements and lack of any road network. The study area belongs to the South

Siberian mountain forest zone, the Altai-Sayan Mountain Conifer Forests Ecoregion, and is characterized by mid-mountain relief with altitudes of 400–800 m above sea level.

The forests are dominated by Siberian fir and Siberian pine (so-called dark coniferous forests). The disturbed forest sites are of feather moss forest types: mesophilic herb/feather moss, blueberry/feather moss, sedge/feather moss and feather moss/shrubs. The study area is dominated by mature and overmature forest stands characterized by average density and forest productivity class [46].

The study area is characterized by a distinctly continental climate that is influenced by humid western air masses in summer and the Siberian anticyclone in winter. The average growing season length is 149–151 days. The coldest month is January (the absolute minimum temperature is minus 50 °C), and the hottest month is July (the absolute maximum temperature is 39 °C). The average annual precipitation is about 530 mm. South-eastern winds prevail (an average speed is 2.8–4.7 m/s) [47].

2.2. Field Studies

2.2.1. Field Research Methods

For estimating tree mortality rate, we placed research plots in stands damaged by the Siberian silkmoth. The field study was based on a methodology developed jointly by scientists from the Sukachev Institute of Forest SB RAS (Krasnoyarsk, Russia) and the Max Planck Institute for Biogeochemistry (Jena, Germany). This methodology is an adaptation of the state forest inventory methodology of the Federal Forestry Agency of the Russian Federation [48]. According to this method, each research plot consists of three concentric circles of constant radius (3.5, 7.5 and 15 m) (Figure 2). The number of trees measured within each circle varies according to their circumference (indicated as C in Figure 2). Trees > 10 cm circumference are to be measured within the first circle; trees >30 cm circumference are to be measured within the second circle, trees >60 cm circumference are to be measured within the third circle. Such a measurement method allows one to reduce effort without a significant loss of accuracy; missing data are restored via extrapolation.

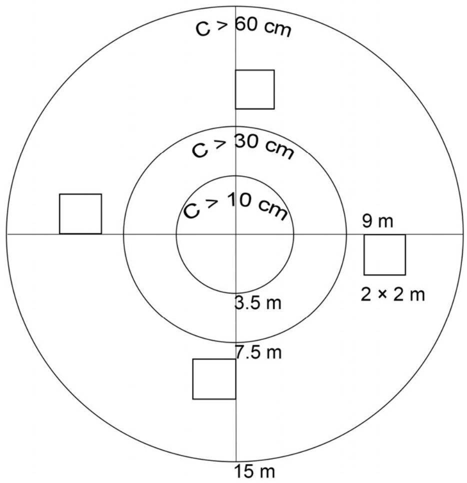

Figure 2. Research plot plan.

For conducting forest inventory on each of the research plots, the following forest stand elements were measured and assessed: trees; young trees, seedling, saplings; large woody debris (LWD); field- and ground-layer vegetation. The litter was also estimated along with field- and ground-layer vegetation biomass, and samples were taken for further estimation of the amount of soil organic matter. Each of the research plots was oriented to the cardinal directions (N, S, W, E) using a compass. The age structure of the forest stands was determined by taking wood cores, or by counting the number of whorls of branches (for young coniferous trees).

For each tree on a research plot, the following metrics are recorded onto the stand measurement sheet: species; trunk circumference at breast height (1.3 m); tree height; height of the base of the live crown; height of the widest crown; condition class; list of damages (if any); tree status (alive/dead); cause of death (for dead trees only). Young trees above 2 m height and <10 cm circumference are measured in the second circle (7.5 m radius). Young trees below 2 m height are measured within four 2 × 2 m quadrats. The quadrats are oriented in cardinal directions and placed at a distance of 9 m from a plot center (Figure 2).

All LWD are measured on each of the research plots (standing dead trees, stumps, lying dead trees, large branches); >5 cm diameter LWD are measured. The following metrics are recorded for LWD: linear dimensions, stage of decomposition, species (if recognizable).

A general description of research plots is also made, including the geographic coordinates of the center point, height above sea level, relief characteristics (aspect, shape of the site, slope angle), soil characteristics (soil type, thickness of organogenic and organomineral horizons), the presence of disturbances (fire, blowdown, insect outbreak, logging, etc.), forest type, stand layers. There are also photographs taken from a plot center: four general-view photographs in the cardinal directions, crown closure, representative photographs of the ground- and field-layer vegetation.

2.2.2. Field Data

When selecting forest stands for placing research plots, we tried to evenly cover the entire damage spectrum—from a few percent disturbance to a stand dieback. The center of a research plot was placed so that the forest site had the same degree of damage at a distance of at least 2 radii of the research plot (30 m) from the center. The minimum distance between the research plots was 120 m. The research plots were places in the second and third year after the end of the outbreak (2022, 2023). A total of 37 research plots were placed in a given area following the method described above (Figure 3b). A relatively low amount of measurements was related to the extreme difficulty of collecting data in the field: there is no way of reaching the edge of the outbreak by car in summer; the outbreak area is stuck with lying dead trees, so travelling there is extremely difficult, traumatic, and takes a long time; another reason is security issues due to wild animals.

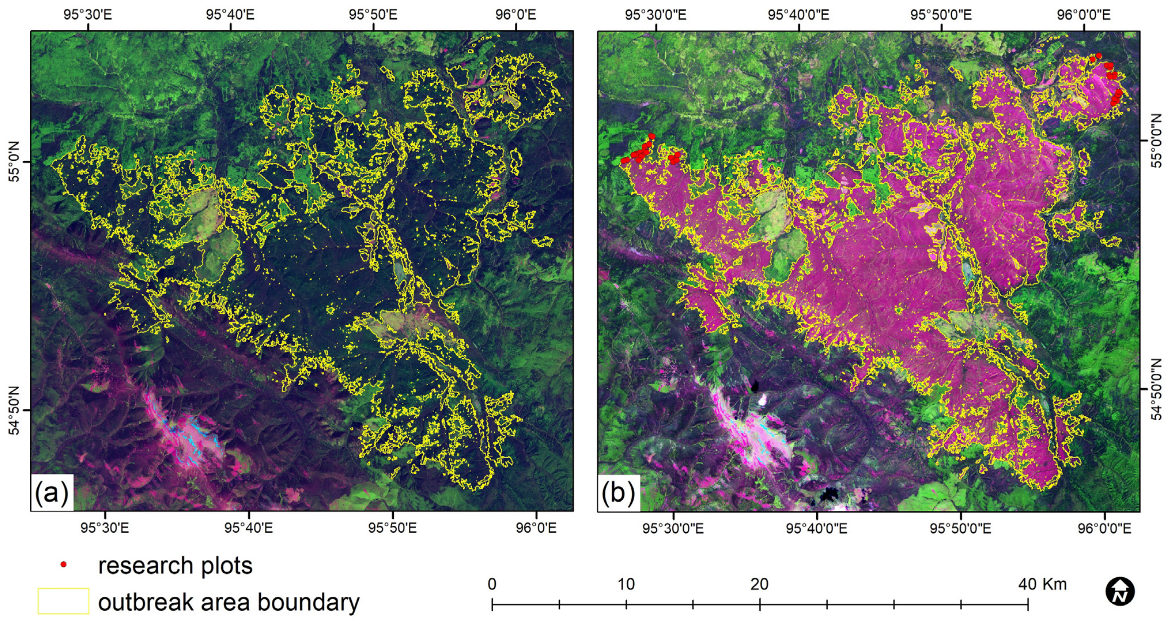

Figure 3. Boundary of the Siberian silkmoth outbreak area from GFW on pre- (**a**) and post-outbreak Sentinel images with research plot distribution (**b**). The false color composite of SWIR-NIR-RED Sentinel-2 bands displays vegetation in colors of green, whereas non-vegetative surfaces are pink or blue.

The processing of data during desk research resulted in determining forest stand characteristics. For estimating tree mortality, we used the data on the growing stock and the stock of standing dead and laying dead trees at the first stage of decomposition (we assumed that these trees died during the outbreak and fall over within five years by the time of the field research) [49–52]. For each research plot, the loss of stem wood relative to its total stock was calculated as a percentage.

2.3. Remote Sensing Data

The boundaries and area of the stands damaged by the Siberian silkmoth (Figure 3) were detected based on the Forest cover loss map from Global Forest Watch dataset 2000–2022 v1.10 (GFW) [53], downloaded from Global Forest Watch Open Data Portal [54]. The GFW dataset is a remote sensing product, based on Landsat time-series imagery that covers latitudes between 80° N and 60° S. It distributes in raster files (GeoTiff) of 10 × 10 degree granules, with a spatial resolution of 30 m. Forest cover loss is defined as a mask of stand-replacement disturbance, or a change from forest to non-forest state for 2000–2022. For the temperate and the boreal biomes, user's and producer's accuracies of forest cover loss are 88% and 94%, respectively [53].

The Forest cover lost map from GFW contains annual data on forest losses from different causes. In order to determine the losses from the silkmoth outbreak in the study area, layers of losses were used only for 2019–2021 (the years of the stands' destruction caused by the silkmoth outbreak) within the borders of Irbeysky district. The absence of fire losses in 2019–2021 was confirmed by the absence of hotspot polygons in the MODIS BurnedArea Product (MCD64A1 v6.1) [55], downloaded from USGS EarthExplorer [56]. Losses from felling are excluded by detecting them using a combination of spectral, textural and border geometry features. The resulting outbreak area boundary is obtained by aggregating polygons from the 2019 to 2021 loss map layers that have contacting borders.

The condition of disturbed stands was determined based on the data from Sentinel-2A and 2B satellites, each carrying a multispectral scanner MSI (spectral bands for MSI are listed in Table 1). Sentinel-2 data were downloaded from the Copernicus Open Access Hub [57].

Table 1. Spectral bands for Sentinel-2 MSI sensors.

Band/Spectral Range	Sentinel-2A	Sentinel-2B	Spatial Resolution (m)
	Central Wavelength (nm)		
1/ Coastal Aerosol (COASTAL BLUE)	422.7	422.3	60
2/ Visible Blue (BLUE)	492.7	492.3	10
3/ Visible Green (GREEN)	559.8	558.9	10
4/ Visible Red (RED)	664.6	664.9	10
5/ Vegetation Read Edge (RE1)	704.1	703.8	20
6/ Vegetation Read Edge (RE2)	740.5	739.1	20
7/ Vegetation Read Edge (RE3)	782.8	779.7	20
8/ Near Infrared (NIR)	832.8	832.9	10
8a/ Narrow Near-Infrared (RE4)	864.7	864	20
9/ Water Vapor	945.1	943.2	60
10/ Cirrus Short Wave Infrared (SWIR)	1373.5	1376.9	60
11/ Short Wave Infrared (SWIR1)	1613.7	1610.4	20
12/ Short Wave Infrared (SWIR2)	2202.4	2185.7	20

The scenes were selected so that to assess the state of forest stands before and after disturbances. The scenes used are cloud-free images closest to the outbreak period: the pre-outbreak scene was acquired in June 2018; post-outbreak scenes were acquired between August 2020 and August 2023. Table 2 shows the list of images acquired during the growing season. All images had a 2A processing level, which includes radiometric, geometric, and atmospheric corrections.

Table 2. List of satellite images used.

Scene ID	Scene Date	Satellite
S2A_MSIL2A_20180625T045701_N9999_R119_T46UFF/T46UFG	25 June 2018	Sentinel 2A
S2A_MSIL2A_20200810T044711_N0214_R076_T46UFF/T46UFG	10 August 2020	Sentinel 2A
S2A_MSIL2A_20200922T045701_N0214_R119_T46UFF/T46UFG	22 September 2020	Sentinel 2A
S2B_MSIL1C_20210601T044659_N0300_R076_T46UFF/T46UFG	1 June 2021	Sentinel 2B
S2B_MSIL2A_20210704T045659_N0301_R119_T46UFF/T46UFG	4 July 2021	Sentinel 2B
S2A_MSIL2A_20210828T045701_N0301_R119_T46UFF/T46UFG	28 August 2021	Sentinel 2A
S2A_MSIL2A_20211017T045811_N0500_R119_T46UFF/T46UFG	17 October 2021	Sentinel 2A
S2A_MSIL1C_20220512T044701_N0400_R076_T46UFF/T46UFG	12 May 2022	Sentinel 2A
S2A_MSIL1C_20220611T044711_N0400_R076_T46UFF/T46UFG	11 June 2022	Sentinel 2A
S2B_MSIL2A_20220808T045659_N0400_R119_ T46UFF/T46UFG	8 August 2022	Sentinel 2B
S2A_MSIL2A_20220919T044711_N0400_R076_ T46UFF/T46UFG	19 September 2022	Sentinel 2A
S2A_MSIL1C_20230616T044701_N0509_R076_T46UFF/T46UFG	16 June 2023	Sentinel 2A
S2A_MSIL1C_20230825T044701_N0509_R076_T46UFF/T46UFG	25 August 2023	Sentinel 2A

Surface reflectance (bottom of atmosphere) values were calculated from the image digital numbers as follows [58]:

$$\text{L2A\_SRi} = \text{L2A\_DNi}/\text{QUANTIFICATION\_VALUEi}, \tag{1}$$

$$\text{L2A\_SRi} = (\text{L2A\_DNi} + \text{BOA\_ADD\_OFFSETi})/\text{QUANTIFICATION\_VALUEi}, \tag{2}$$

where L2A_SRi—surface reflectance value, L2A_DNi—image digital number, QUANTIFICATION_VALUEi—in order to convert digital number into reflectance, initially set to 10,000, BOA_ADD_OFFSETi—radiometric offset value, initially set to −1000 digital counts for all the bands.

The BOA_ADD_OFFSET and QUANTIFICATION_VALUE could be found in the product metadata file.

For images acquired before 25 January 2022, surface reflectance values were calculated using Equation (1), after this date—using Equation (2), due to Sentinel-2 processing baseline 04.00 deployment.

2.4. Methods

Among the wide range of existing remote sensing indices described in the literature, we selected and estimated the effectiveness for assessing tree mortality of the following: NDVI, dNDVI, NBR, dNBR, NDMI, EVI, TCG. This choice was due to their effectiveness in assessing forests disturbed by various types of defoliators, showed by other researchers. Table 3 shows formulas used to calculate these indices and Sentinel-2 bands used.

Table 3. Calculation algorithms with used Sentinel-2 bands.

Index	Formula	Reference
NDVI (Normalized Difference Vegetation Index)	(NIR − RED)/(NIR + RED)	Tucker, 1979 [59]
dNDVI (difference in Normalized Difference Vegetation Index)	NDVIpre − NDVIpost	Zhu et al., 2006 [60]
NBR (Normalized Burn Ratio)	(NIR − SWIR2)/(NIR + SWIR2)	Key et al., 2002 [61]
dNBR (difference in Normalized Burn Ratio)	NBRpre − NBRpost	Key, 2006 [62]
NDMI (Normalized Difference Moisture Index)	(NIR − SWIR1)/(NIR + SWIR1)	Gao, 1996 [63]
EVI (Enhanced Vegetation Index)	2.5(NIR − RED)/(NIR + 6RED − 7.5BLUE) + 1	Gao et al., 2000 [64]
TCG (Tasseled Cap Greenness)	−0.28482BLUE − 0.24353GREEN − 0.54364RED + 0.72438NIR + 0.084011SWIR1 − 0.180012SWIR2	Crist et al., 1984 [65]

Sentinel-2 imagery processing, vector data processing, and cartography were performed by means of ESRI ArcGIS Desktop v10.5. Using this software, all indices presented in Table 3 were calculated for each Sentinel-2 scene (listed earlier in Table 2). Thus, a set of seven indices was obtained for each Sentinel-2 image. The coordinates of the research plot centers were uploaded to ArcGIS from GPS data. The index values were extracted for the points corresponding to the centers of the research plots.

Statistical processing of the obtained datasets was performed using the R caret package [66]. Linear regression models were built that connected the values of remote sensing indices with the tree mortality rate measured during the field study. Tree mortality value was used as a response variable in the regression. This procedure resulted in seven models per each date.

The validity of the regression models was verified using the repeated k-fold cross-validation method [67]. According to the k-fold cross-validation method, the dataset is randomly divided into k-subsets (or k-fold). One subset is reserved for the testing and estimating the prediction error, and all other subsets are used for the model building. The process is repeated until each of the k-subsets has served as the test set. After that, the average of k recorded errors is calculated. The repeated k-fold cross-validation method reiterates the splitting of data into k-folds several times. The final model error is taken as the mean error from the number of repeats.

We used k = 5 because of the small size of our dataset (37 measurements), and the number of repeats is 5. According to the selected model parameters, training subsets consisted of 29 or 30 measurements, validation subsets were 7 or 8 measurements.

Coefficients of determination R-squared (R^2) and significance levels (p) were determined to assess the quality of regression models.

As a result, we identified the regression model with the highest R^2 value combined with the lowest root mean squared error (RMSE) and mean absolute error (MAE) values. It was used to recalculate index values into tree mortality values for the entire outbreak area. As a result, for each pixel of the image, we obtained the value of the tree mortality in the range from 0 to 100 percent, in increments of 1 percent.

3. Results

Linear regression models were built for a set of seven indices, calculated for every 12 Sentinel-2 scenes used in the research. Thus, 84 regression models were built. Performance of the models was assessed using a 5-fold cross-validation method repeated five times. RMSE, MAE, and R^2 were used as performance metrics for the regression.

Most of the indices tested in our research correlated well with the field measurements of tree mortality. Table 4 shows the coefficients of determination R^2, significance levels, as well as the RMSE, and MAE errors for linear regression models. Significance levels $p < 0.001$ are unmarked, and $p < 0.01$ are marked with *.

Table 4. Coefficients of determination R^2, significance of linear regression models and accuracy assessments.

Date	Accuracy	NDVI	dNDVI	NBR	dNBR	NDMI	EVI	TCG
10 August 2020	R^2	0.623	0.662	0.749	0.712	0.710	0.584	0.564
	RMSE	17.962	17.663	15.775	15.908	15.605	20.888	20.268
	MAE	15.500	15.081	13.597	13.833	13.287	17.835	17.177
22 September 2020	R^2	0.820	0.848	0.872	0.855	0.866	0.826	0.839
	RMSE	13.126	12.936	11.427	11.897	11.572	15.018	14.871
	MAE	11.258	10.876	9.602	10.524	9.949	12.016	11.920
1 June 2021	R^2	0.539	0.624	0.670	0.715	0.635	0.504	0.558
	RMSE	20.609	19.451	18.161	16.891	18.455	21.759	21.040
	MAE	17.260	16.083	15.807	14.846	16.077	18.939	18.054
4 July 2021	R^2	0.635	0.614	0.699	0.715	0.635	0.340 *	0.325 *
	RMSE	19.930	19.058	16.995	16.891	18.455	25.820	25.263
	MAE	16.896	16.366	14.982	14.846	16.077	22.401	22.088
28 August 2021	R^2	0.742	0.769	0.851	0.840	0.841	0.696	0.669
	RMSE	15.442	14.506	12.490	12.455	12.530	18.566	17.703
	MAE	12.531	11.892	10.452	10.700	10.331	14.875	14.157

Table 4. *Cont.*

Date	Accuracy	NDVI	dNDVI	NBR	dNBR	NDMI	EVI	TCG
17 October 2021	R^2	0.712	0.703	0.626	0.581	0.603	0.695	0.699
	RMSE	16.732	15.855	18.909	20.121	20.300	17.944	17.115
	MAE	14.059	12.688	16.706	16.933	17.140	15.155	14.747
12 May 2022	R^2	0.703	0.692	0.790	0.797	0.796	0.722	0.733
	RMSE	17.335	17.088	14.223	13.533	14.445	16.322	15.799
	MAE	14.310	13.748	11.973	11.316	12.117	13.216	12.784
11 June 2022	R^2	0.750	0.768	0.766	0.773	0.716	0.509	0.500
	RMSE	15.376	14.883	15.181	14.872	15.732	22.107	21.781
	MAE	12.439	11.805	12.691	12.814	12.953	18.021	17.904
8 August 2022	R^2	0.791	0.779	0.809	0.768	0.809	0.627	0.661
	RMSE	14.486	14.044	13.866	14.419	13.456	19.329	19.157
	MAE	11.711	11.091	11.796	12.494	11.492	15.723	15.362
19 September 2022	R^2	0.721	0.720	0.847	0.849	0.851	0.761	0.774
	RMSE	15.823	15.668	12.412	12.507	12.137	14.683	15.056
	MAE	12.465	12.354	10.134	10.502	9.629	11.539	11.971
16 June 2023	R^2	0.697	0.690	0.693	0.665	0.720	0.417	0.443
	RMSE	17.324	17.391	17.275	17.809	16.762	24.659	23.888
	MAE	13.906	13.694	14.810	15.484	14.201	21.249	20.526
25 August 2023	R^2	0.704	0.710	0.802	0.791	0.800	0.554	0.583
	RMSE	16.461	16.802	13.152	13.751	13.649	21.135	20.672
	MAE	13.483	13.801	10.302	11.483	10.569	16.454	16.027

Significance levels $p < 0.001$ are unmarked, and $p < 0.01$ are marked with *.

NBR, NDMI and dNBR indices estimate tree mortality with high accuracy, except for the middle of the growing season and the late autumn scene dates. All other indices NDVI, dNDVI, EVI and TCG show high or moderate accuracy, depending on the scene date. The best results for all indices were obtained for a scene taken shortly after the end of the outbreak (22 September 2020).

The NBR index, calculated for the image of 22 September 2020, showed the highest R^2 value between the satellite and field data, and the lowest RMSE and MAE. Therefore, we used a linear regression model built for this index (Figure 4) to recalculate the index values into tree mortality values.

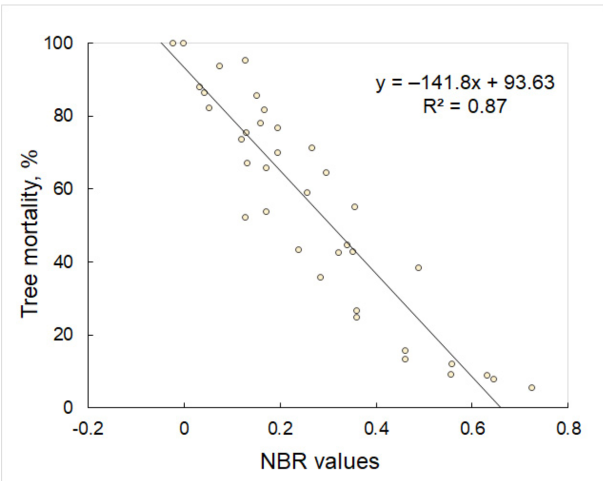

Figure 4. The relationship between field measurements of tree mortality and the NBR remote sensing index. The regression line is shown in black. The linear regression model equation and the coefficient of determination are shown at the top of the diagram.

As a result, we determined a tree mortality percentage for each pixel (10 × 10 m) of a satellite image within the Siberian silkmoth outbreak area. Figure 5 shows the resulting tree mortality map in 10% interval groups.

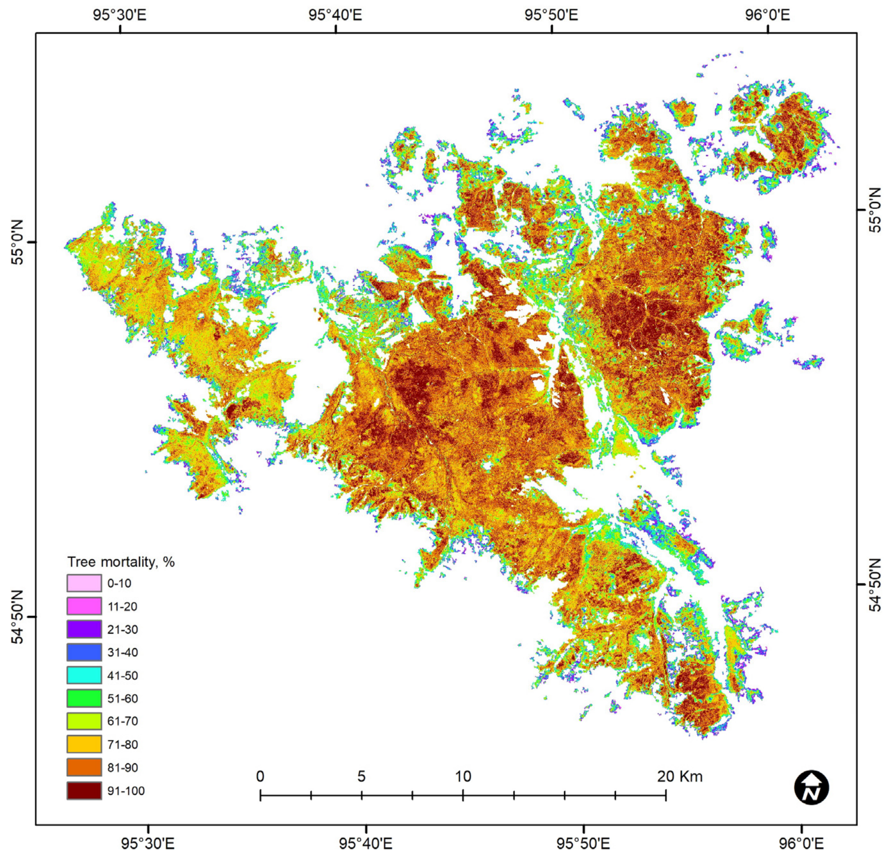

Figure 5. Mapping tree mortality using NBR index.

Figure 6 shows the area occupied by stands characterized by different tree mortality rates. The data on tree mortality are grouped in class intervals of 10%, as shown in Figure 5. The areas are represented in the following ways: absolute area values (in ha), and the proportion that stands of different mortality rates take in the total outbreak area (in %).

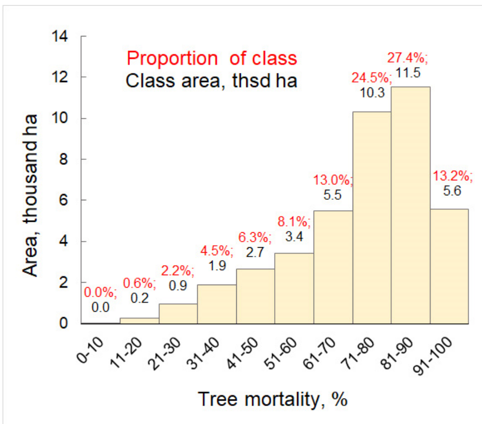

Figure 6. Histogram representing tree mortality by 10% mortality intervals, with area in thousand hectares (in black) and proportion of individual classes (in red).

It was discovered that the area disturbed by the Siberian silkmoth is dominated by forests characterized by high tree mortality values. Indicatively, about 80% of the outbreak area is covered by stands characterized by more than 60% tree mortality.

4. Discussion

The present research investigate the use of Sentinel-2 imagery to quantify the condition of forest stands disturbed by coniferous defoliator—Siberian silkmoth. Sentinel-2 imagery refers to medium spatial resolution remote sensing data, that have previously been successfully used to assess the insect damage severity by both bark beetles [31,32,34–37] and defoliators [31,33,36,68,69]. The originality of our research derived from using Sentinel-2 imagery for quantitative assessments of tree mortality in dark coniferous taiga forests disturbed by Siberian silkmoth outbreak. As a result, we found that Sentinel imagery can be used to solve this issue effectively.

A number of spectral indices, such as NDVI, dNDVI, NBR, dNBR, NDMI, EVI and TCG, are widely used to solve similar tasks [31–42,69,70]. Finally, we revealed that all these indices correlated well with the field measurements of tree mortality for images taken shortly after the end of the outbreak. Results also indicated that NBR was the best single-image index to detect tree mortality in the study area. In general, indices based on NIR/SWIR bands (NBR, NDMI, dNBR) demonstrate the best correlations with tree mortality compared with indices using VISIBLE/NIR or VISIBLE/NIR/SWIR bands (NDVI, dNDVI, EVI, TCG) (Table 4). Rahimzadeh-Bajgiran [63] discovered that NDMI was the best index to detect defoliation caused by spruce budworm across the Canadian boreal forests, that corresponds to our results. Actually, there are not many studies regarding the use of spectral indices to assess the severity of coniferous defoliators. However, those for broadleaf defoliators confirm our results, showing that NIR/SWIR-based indices are preferred to VIS/NIR indices for mapping insect disturbances [70–72].

The highest correlations between satellite and field data on tree mortality were obtained for indices calculated from images obtained shortly after the end of the Siberian silkmoth outbreak (Table 4). This is explained by the fact that soon after canopy dieback, ground- and field-layer plants receive much more sunlight and water, which results in their rapid growth. Thus, there is an increase in the values of photosynthetic activity in disturbed areas the very next year after tree dieback. This effect has been described in some research papers [18,19,28]. The same reasons can most likely explain why the correlations for images of the beginning and the end of the growing season are higher than for the middle: the absence of the contribution of herbs and shrubs to the albedo values allows the state of the forest stand to be assessed more accurately.

It was also found that using a pair of images before/after the outbreak does not lead to an increase in correlation compared to single images taken shortly after the end of the outbreak.

In addition, there is a trend towards a decrease in correlation between satellite and field data on tree mortality as the time between a disturbance and an imaging date increases. In this regard, the main limitation of our methodology is the availability of satellite images taken shortly after the disturbance at the end of the growing season. Difficulties in obtaining such images may be associated with the presence of clouds due to frequent rain in this season.

However, a few years after the end of the outbreak, NBR, NDMI and dNBR indices still demonstrate good applicability for estimating tree mortality, especially for the images obtained at the end of the growing season (Table 4).

The need to collect data in the field, associated with the increase in time required and financial costs, is another limitation of the proposed methodology. Unfortunately, we cannot yet unify the proposed models for estimating tree mortality for different territories damaged by outbreaks of the Siberian silkmoth. Within Krasnoyarsk Krai, large disturbed areas require similar assessments. Thus, our future research will be aimed at finding a solution to this problem.

It should also be mentioned that the MSI sensor has four red edge bands specially developed for monitoring vegetation's health. In the present research, we have not used any indices based on the red edge bands, because we focused on investigating the use of universal indices. However, we are planning separate research for indices based on MSI red edge bands, such as FAPAR (fraction of absorbed photosynthetically active radiation), LAI (leaf area index), CCC (canopy chlorophyll content) and CWC (canopy water content).

5. Conclusions

We revealed a number of spectral indices calculated from Sentinel satellite data that enable one to conduct high-reliability quantification of the state of forest stands disturbed by Siberian silkmoth outbreaks. This will make it possible to assess carbon emission release from the decomposition of dead trees, which is crucial for studying the carbon cycle and global climate change. What is more, the results of the present research can be used in forestry as a fundamental basis in decision-making for fire prevention measures, sanitation cutting, artificial reforestation, etc., in forests damaged by the Siberian silkmoth.

Author Contributions: Conceptualization, O.A.S., P.V.M. and A.I.T.; methodology, O.A.S. and P.V.M.; validation, O.A.S. and N.P.K.; formal analysis, O.A.S., S.M.S., D.A.D. and A.I.T.; investigation, O.A.S. and D.A.D.; resources, O.A.S. and N.P.K.; data curation, O.A.S. and P.V.M.; writing—original draft preparation, O.A.S.; writing—review and editing, O.A.S., D.A.D. and A.I.T.; project administration, S.M.S.; funding acquisition, P.V.M. and S.M.S. All authors have read and agreed to the published version of the manuscript.

Funding: The research was carried out within the projects "Fundamentals of forest protection from entomo- and fittings pests in Siberia" (№ FEFE-2020-0014) within the framework of the state assignment, set out by the Ministry of Education and Science of the Russian Federation, for the implementation by the Scientific Laboratory of Forest Health.

Data Availability Statement: The data presented in this study are available on request from the corresponding author.

Acknowledgments: We would like to thank the Krasnoyarsk center for the collective use of the Federal research center of the Siberian branch of the Russian Academy of Sciences for the equipment provided. We thank Victor Ilyin for his help with data processing automation. We would also like to thank Reviewer2 for the helpful and insightful comments that significantly improved the quality of the manuscript.

Conflicts of Interest: The authors declare no conflict of interest.

References

1. Gauthier, S.; Bernier, P.; Kuuluvainen, T.; Shvidenko, A.Z.; Schepaschenko, D.G. Boreal forest health and global change. *Science* **2015**, *349*, 819–822. [CrossRef] [PubMed]
2. Dixon, R.K.; Brown, S.; Houghton, R.A.; Solomon, A.M.; Trexler, M.C.; Wisniewski, J. Carbon Pools and Flux of Global Forest Ecosystems. *Science* **1994**, *263*, 185–190. [CrossRef]
3. Masson-Delmotte, V.; Zhai, P.; Pirani, A.; Connors, S.L.; Péan, C.; Berger, S.; Caud, N.; Chen, Y.; Goldfarb, L.; Gomis, M.I. Contribution of Working Group I to the Sixth Assessment Report of the Intergovernmental Panel on Climate Change. In *Climate Change 2021: The Physical Science Basis*; Cambridge University Press: Cambridge, UK; New York, NY, USA, 2021. [CrossRef]
4. Flannigan, M.D.; Logan, K.A.; Amiro, B.D.; Skinner, W.R.; Stocks, B.J. Future Area Burned in Canada. *Clim. Chang.* **2005**, *72*, 1–16. [CrossRef]
5. Williams, N.G.; Lucash, M.S.; Ouellette, M.R.; Brussel, T.; Gustafson, E.; Weiss, S.A.; Sturtevant, B.R.; Shchepashchenko, D.; Shvidenko, A. Simulating dynamic fire regime and vegetation change in a warming Siberia. *Fire Ecol.* **2023**, *19*, 33. [CrossRef]
6. Kurz, W.A.; Stinson, G.; Rampley, G.J.; Dymond, C.C.; Neilson, E.T. Risk of natural disturbances makes future contribution of Canada's forests to the global carbon cycle highly uncertain. *Proc. Natl. Acad. Sci. USA* **2008**, *105*, 1551–1555. [CrossRef] [PubMed]
7. Boldaruev, V.O. Results and prospects for the study and extermination of the *Siberian silkmoth* in Eastern Siberia. In *Materials on the Problem of the Siberian silkmoth*; Publishing House of Siberian Brach of USSR Academy of Science: Novosibirsk, Russia, 1960; pp. 3–10.
8. Galkin, G.I. Some issues of the formation of reservations and primary outbreak spots of the *Siberian silkmoth* in Krasnoyarsk Krai forests. In *Siberian Silkmoth*; Publishing House of Siberian Brach of USSR Academy of Science: Novosibirsk, Russia, 1960; pp. 21–33.
9. Kharuk, V.I.; Antamoshkina, O.A. Impact of Silkmoth Outbreak on Taiga Wildfires. *Contemp. Probl. Ecol.* **2017**, *10*, 556–562. [CrossRef]
10. Fajvan, M.A.; Wood, J.M. Stand structure and development after gypsy moth defoliation in the Appalachian Plateau. *For. Ecol. Manag.* **1996**, *89*, 79–88. [CrossRef]

11. Janes, J.K.; Li, Y.; Keeling, C.I.; Yuen, M.M.S.; Boone, C.K.; Cooke, J.E.K.; Bohlmann, J.; Huber, D.P.W.; Murray, B.W.; Coltman, D.W.; et al. How the mountain pine beetle (*Dendroctonus ponderosae*) breached the canadian rocky mountains. *Mol. Biol. Evol.* **2014**, *31*, 1803–1815. [CrossRef]
12. Quirion, B.R.; Domke, G.M.; Walters, B.F.; Lovett, G.M.; Fargione, J.E.; Greenwood, L.; Serbesoff-King, K.; Randall, J.M.; Fei, S. Insect and Disease Disturbances Correlate With Reduced Carbon Sequestration in Forests of the Contiguous United States. *Front. For. Glob. Chang.* **2021**, *4*, 716582. [CrossRef]
13. Lehmann, P.; Ammunét, T.; Barton, M.; Battisti, A.; Eigenbrode, S.D.; Jepsen, J.U.; Kalinkat, G.; Neuvonen, S.; Niemelä, P.; Terblanche, J.S.; et al. Complex responses of global insect pests to climate warming. *Front. Ecol. Environ.* **2020**, *18*, 141–150. [CrossRef]
14. Kharuk, V.I.; Im, S.T.; Yagunov, M.N. Migration of the Northern Boundary of the Siberian Silk Moth. *Contemp. Probl. Ecol.* **2018**, *11*, 26–34. [CrossRef]
15. Anderegg, W.R.L.; Hicke, J.A.; Fisher, R.A.; Allen, C.D.; Aukema, J.; Bentz, B.; Hood, S.; Lichstein, J.W.; Macalady, A.K.; Mcdowell, N.; et al. Tree mortality from drought, insects, and their interactions in a changing climate. *New Phytol.* **2015**, *208*, 674–683. [CrossRef] [PubMed]
16. Kondakov, Y.P. The outbreaks of Siberian silk moth in Krasnoyarsk krai forests. In *Entomological Researches in Siberia*; KF RES: Krasnoyarsk, Russia, 2002; Volume 2, pp. 25–74.
17. Epova, V.I.; Pleshanov, A.S. *Zones of Severity of Phyllophagous Insects in Asian Russia*; Nauka, Siberian Publishing House RAS: Novosibirsk, Russia, 1995; p. 47.
18. Kolomiets, N.G. Siberian silkworm—A pest of the lowland taiga. In *Proceedings on Forestry of Western Siberia*; Nauka: Novosibirsk, Russia, 1957; Volume 3, pp. 61–76.
19. Kondakov, Y.P. Mass reproduction of Siberian silk moth. In *Ekologiya Populyatsii Lesnykh Zhivotnykh Sibiri (Population Ecology of Forest Animals in Siberia)*; Nauka: Novosibirsk, Russia, 1974; pp. 206–264.
20. Grodnitsky, D.L. Siberian silkworm and the fate of fir taiga. *Nature* **2004**, *11*, 49–56.
21. Pavlov, I.N.; Litovka, Y.A.; Golubev, D.V.; Astapenko, S.A.; Chromogin, P.V. New outbreak of *Dendrolimus sibiricus* tschetv. in Siberia (2012–2017): Monitoring, modeling and biological control. *Contemp. Probl. Ecol.* **2018**, *11*, 406–419. [CrossRef]
22. Furyaev, V.V. *Forests That Died after Siberian Silk Moth Outbreaks and Thier Prescribed Burning*; Nauka: Moskow, Russia, 1966.
23. Isaev, A.S.; Palnikova, E.N.; Sukhovolsky, V.G.; Tarasova, O.V. *Population Dynamics of Defoliating Forest Insects: Models and Forecasts*; KMK Scientific Press Ltd.: Moscow, Russia, 2015; p. 262.
24. Isaev, A.S.; Soukhovolsky, V.G.; Tarasova, O.V.; Palnikova, E.N.; Kovalev, A.V. *Forest Insect Population Dynamics, Outbreaks and Global Warming Effects*; Wiley: Hoboken, NJ, USA, 2017; 298p.
25. Soukhovolsky, V.G.; Kovalev, A.V.; Palnikova, E.N.; Tarasova, O.V. Modelling the risk of insect impacts on forest stands after possible climate changes. *Comput. Stud. Model.* **2016**, *8*, 241–253. [CrossRef]
26. Demidko, D.A.; Goroshko, A.A.; Slinkina, O.A.; Mikhaylov, P.V.; Sultson, S.M. The Role of Forest Stands Characteristics on Formation of Exterior Migratory Outbreak Spots by the Siberian Silk Moth *Dendrolimus sibiricus* (Tschetv.) during Population Collapse. *Forests* **2023**, *14*, 1078. [CrossRef]
27. Franklin, J.F.; Lindenmayer, D.B.; MacMahon, J.A.; McKee, A.; Magnusson, J.; Perry, D.A.; Waide, R.; Foster, D. Threads of continuity: Ecosystems disturbances, biological legacies, and ecosystem recovery. *Conserv. Biol. Pract.* **2000**, *1*, 8–17. [CrossRef]
28. Valendik, E.N.; Verkhovets, S.V.; Kisilyakhov, E.K.; Lantukh, A.Y. The role of forests damaged by the *Siberian silkmoth* in forest fires in the Lower Angara region. *For. Manag.* **2004**, *6*, 27–29.
29. Jonášová, M.; Prach, K. The Influence of Bark Beetles Outbreak vs. Salvage Logging on Ground Layer Vegetation in Central European Mountain Spruce Forests. *Biol. Conserv.* **2008**, *141*, 1525–1535. [CrossRef]
30. Niemelä, J. Management in Relation to Disturbance in the Boreal Forest. *For. Ecol. Manag.* **1999**, *115*, 127–134. [CrossRef]
31. Davis, S.M.; Landgrebe, D.A.; Phillips, T.L.; Swain, P.H.; Hoffer, R.M.; Lindenlaub, J.C.; Silva, L.F. *Remote Sensing: The Quantitative Approach*; McGraw-Hill International Book Co.: New York, NY, USA, 1978.
32. Vygodskaya, I.N.; Gorshkova, I.I. *Theory and Experiment in Remote-Sensing Studies of Vegetation*; Gidrometeoizdat: Moscow, Russia, 1987; p. 246.
33. Kronberg, P. *Remote-Sensing Study of the Earth*; Mir: Moscow, Russia, 1988; p. 350.
34. Senf, C.; Seidl, R.; Hostert, P. Remote sensing of forest insect disturbances: Current state and future directions. *Int. J. Appl. Earth Obs. Geoinform.* **2017**, *60*, 49–60. [CrossRef] [PubMed]
35. Meng, R.; Gao, R.; Zhao, F.; Huang, C.; Sun, R.; Lv, Z.; Huang, Z. Landsat-based monitoring of southern pine beetle infestation severity and severity change in a temperate mixed forest. *Remote Sens. Environ.* **2022**, *269*, 112847. [CrossRef]
36. Long, J.; Lawrence, R. Mapping Percent Tree Mortality Due to Mountain Pine Beetle Damage. *For. Sci.* **2016**, *62*, 392–402. [CrossRef]
37. Havašová, M.; Bucha, T.; Ferenčík, J.; Jakuš, R. Applicability of a vegetation indices-based method to map bark beetle outbreaks in the High Tatra Mountains. *Ann. For. Res.* **2015**, *58*, 295–310. [CrossRef]
38. Meddens, A.J.H.; Hicke, J.A.; Vierling, L.A.; Hudak, A.T. Evaluating methods to detect bark beetle-caused tree mortality using single-date and multi-date Landsat imagery. *Remote Sens. Environ.* **2013**, *132*, 49–58. [CrossRef]
39. Meigs, G.W.; Kennedy, R.E.; Cohen, W.B. A Landsat time series approach to characterize bark beetle and defoliator impacts on tree mortality and surface fuels in conifer forests. *Remote Sens. Environ.* **2011**, *115*, 3707–3718. [CrossRef]

40. Hart, S.J.; Veblen, T.T. Detection of Spruce Beetle-Induced Tree Mortality Using High- and Medium-Resolution Remotely Sensed Imagery. *Remote Sens. Environ.* **2015**, *168*, 134–145. [CrossRef]
41. Kharuk, V.I.; Ranson, K.J.; Kozuhovskaya, A.G.; Kondakov, Y.P.; Pestunov, I.A. NOAA/AVHRR satellite detection of *Siberian silkmoth* outbreaks in eastern Siberia. *Int. J. Remote Sens.* **2004**, *25*, 5543–5555. [CrossRef]
42. Ershov, D.V.; Devyatova, N.V. Application of satellite survey data to monitor mass outbreaks of Siberian moth. *Izv. Vyssh. Uchebn. Zaved. Geod. Aerofotos'emka* **2008**, *2*, 161–167.
43. Fassnacht, F.E.; Latifi, H.; Ghosh, A.; Joshi, P.K.; Koch, B. Assessing the potential of hyperspectral imagery to map bark beetle-induced tree mortality. *Remote Sens. Environ.* **2014**, *140*, 533–548. [CrossRef]
44. Hicke, J.A.; Logan, J. Mapping whitebark pine mortality caused by a mountain pine beetle outbreak with high spatial resolution satellite imagery. *Int. J. Remote Sens.* **2009**, *30*, 4427–4441. [CrossRef]
45. Coops, N.C.; Johnson, M.; Wulder, M.A.; White, J.C. Assessment of QuickBird high spatial resolution imagery to detect red attack damage due to mountain pine beetle infestation. *Remote Sens. Environ.* **2006**, *103*, 67–80. [CrossRef]
46. Smagin, V.N.; Ilinskaya, S.A.; Nazimova, D.I.; Novoseltseva, I.F.; Cherednikova, J.S. *Forest Types of Mountains of Southern Siberia*; Nauka: Novosibirsk, Russia, 1980; p. 336.
47. Polikarpov, N.P.; Chebakova, N.M.; Nazimova, D.I. *Climate and Mountain Forests in Southern Siberia*; Nauka: Novosibirsk, Russia, 1986; p. 225.
48. *Order of Federal Forestry Agency on Approval of the Regulations for Organizing and Carrying Out Activities for State Forest Inventory*; Federal Forestry Agency, Its Territorial Authorities and Subordinate Organizations: Moscow, Russia, 2022.
49. Zhuravlev, P.G. *Recommendations for Siberian Silkworm Control in the Forests of Russian Far East*; FEFRI: Khabarovsk, Russia, 1960; p. 33.
50. Grodnitsky, D.L.; Raznobarsky, V.G.; Soldatov, V.V.; Remarchuk, N.P. Degradation of taiga forests disturbed by the *Siberian silkmoth*. *Contemp. Probl. Ecol.* **2002**, *1*, 3–12.
51. Baranchikov, Y.N.; Perevoznikova, V.D. The *Siberian silkmoth* outbreak areas as a source of additional carbon emissions. In *Readings in Memory of Academician V. N. Sukachev. XX. Insects in Forest Biogeocenoses*; KMK Scientific Press Ltd. Publishing House: Moscow, Russia, 2004; pp. 32–53.
52. Krivolutskaya, G.O. *Secretive Stem Pests in Dark Coniferous Forests Damaged by the Siberian Silkmoth in Western Siberia*; Nauka: Moscow, Russia, 1965; p. 130.
53. Forest Cover Loss Map from Global Forest Watch Dataset v1.10. Available online: https://data.globalforestwatch.org/ (accessed on 2 September 2023).
54. Hansen, M.C.; Potapov, P.V.; Moore, R.; Hancher, M.; Turubanova, S.A.; Tyukavina, A.; Thau, D.; Stehman, S.V.; Goetz, S.J.; Loveland, T.R.; et al. High-Resolution Global Maps of 21st-Century Forest Cover Change. *Science* **2013**, *342*, 850–853. [CrossRef] [PubMed]
55. Giglio, L.; Boschetti, L.; Roy, D.P.; Humber, M.L.; Justice, C.O. The Collection 6 MODIS burned area mapping algorithm and product. *Remote Sens. Environ.* **2018**, *217*, 72–85. [CrossRef]
56. USGS Earthexplorer. Available online: https://earthexplorer.usgs.gov/ (accessed on 14 August 2023).
57. Copernicus Open Access Hub. Available online: https://scihub.copernicus.eu (accessed on 2 September 2023).
58. Sentinel Online. Sentinel-2 Annual Performance Report—Year 2022. Available online: https://sentinels.copernicus.eu/ca/web/sentinel/user-guides/sentinel-2-msi/document-library (accessed on 21 September 2023).
59. Tucker, C.J. Red and photographic infrared linear combinations for monitoring vegetation. *Remote Sens. Environ.* **1979**, *8*, 127–150. [CrossRef]
60. Zhu, Z.; Key, C.H.; Ohlen, D.; Benson, N.C. *Evaluate Sensitivities of Burn-Severity Mapping Algorithms for Different Ecosystems and Fire Histories in the United States*; Final Report to the Joint Fire Sciences Program, JFSP 01-1-4-12; Joint Fire Science Program: Boise, IA, USA, 2006.
61. Key, C.H.; Benson, N.; Ohlen, D.; Howard, S.; McKinley, R.; Zhu, Z. The normalized burn ratio and relationships to burn severity: Ecology, remote sensing and implementation. In Proceedings of the Ninth Forest Service Remote Sensing Applications Conference, San Diego, CA, USA, 8–12 April 2002; Greer, J.D., Ed.; American Society for Photogrammetry and Remote Sensing: Bethesda, MD, USA, 2002.
62. Key, C.H. Ecological and sampling constraints on defining landscape fire severity. *Fire Ecol.* **2006**, *2*, 34–59. [CrossRef]
63. Gao, B.-C. NDWI—A normalized difference water index for remote sensing of vegetation liquid water fromspace. *Remote Sens. Environ.* **1996**, *58*, 257–266. [CrossRef]
64. Gao, X.; Huete, A.R.; Ni, W.; Miura, T. Optical–biophysical relationships of vegetation spectra without background contamination. *Remote Sens. Environ.* **2000**, *74*, 609–620. [CrossRef]
65. Crist, E.P.; Cicone, R.C. A physically-based transformation of Thematic Mapper data—The TM Tasseled Cap. *IEEE Trans. Geosci. Remote Sens.* **1984**, *22*, 256–263. [CrossRef]
66. Kuhn, M. Building Predictive Models in R Using the caret Package. *J. Stat. Softw.* **2008**, *28*, 1–26. [CrossRef]
67. Gareth, J.; Witten, D.; Hastie, T.; Tibshirani, R. *An Introduction to Statistical Learning: With Applications in R*; Springer Publishing Company, Incorporated: New York, NY, USA, 2014. [CrossRef]
68. Pasquarella, V.J.; Bradley, B.A.; Woodcock, C.E. Near-Real-Time Monitoring of Insect Defoliation Using Landsat Time Series. *Forests* **2017**, *8*, 275. [CrossRef]

69. Rahimzadeh-Bajgiran, P.; Weiskittel, A.R.; Kneeshaw, D.; MacLean, D.A. Detection of Annual Spruce Budworm Defoliation and Severity Classification Using Landsat Imagery. *Forests* **2018**, *9*, 357. [CrossRef]
70. Townsend, P.A.; Singh, A.; Foster, J.R.; Rehberg, N.J.; Kingdon, C.C.; Eshleman, K.N.; Seagle, S.W. A general Landsat model to predict canopy defoliation in broadleaf deciduous forests. *Remote Sens. Environ.* **2012**, *119*, 255–265. [CrossRef]
71. De Beurs, K.M.; Townsend, P.A. Estimating the effect of gypsy moth defoliation using MODIS. *Remote Sens. Environ.* **2008**, *112*, 3983–3990. [CrossRef]
72. Fraser, R.H.; Latifovic, R. Mapping insect-induced tree defoliation and mortality using coarse spatial resolution satellite imagery. *Int. J. Remote Sens.* **2005**, *26*, 193–200. [CrossRef]